

Multiple-Crop Human Mesh Recovery with Contrastive Learning and Camera Consistency in A Single Image

Yongwei Nie¹, Changzhen Liu¹, Chengjiang Long², Qing Zhang³, Guiqing Li¹, Hongming Cai¹

¹South China University of Technology, China ²Meta Reality Labs, USA

³Sun Yat-sen University, China

{nieyongwei}@scut.edu.cn

Abstract

We tackle the problem of single-image Human Mesh Recovery (HMR). Previous approaches are mostly based on a single crop. In this paper, we shift the single-crop HMR to a novel multiple-crop HMR paradigm. Cropping a human from image multiple times by shifting and scaling the original bounding box is feasible in practice, easy to implement, and incurs neglectable cost, but immediately enriches available visual details. With multiple crops as input, we manage to leverage the relation among these crops to extract discriminative features and reduce camera ambiguity. Specifically, (1) we incorporate a contrastive learning scheme to enhance the similarity between features extracted from crops of the same human. (2) We also propose a crop-aware fusion scheme to fuse the features of multiple crops for regressing the target mesh. (3) We compute local cameras for all the input crops and build a camera-consistency loss between the local cameras, which reward us with less ambiguous cameras. Based on the above innovations, our proposed method outperforms previous approaches as demonstrated by the extensive experiments.

1. Introduction

Since the seminar work of HMR (Human Mesh Recovery) by [19], more and more work attempts to estimate the 3D mesh of a human from a single image, due to its potential applications in VR/AR, virtual try-on and simulative-coaching, etc. The obtained mesh is usually represented by the parametric SMPL model [37] or sometimes by mesh vertices directly [33, 34].

Most of previous work treats this task as a regression problem [6, 19, 28, 30, 54, 64]. They first detect and crop a human from a full-view image, and then send the cropped image to a neural network to output the target mesh together with a camera that projects the mesh to 2D image. However, the task poses two core challenges. First, it demands to ex-

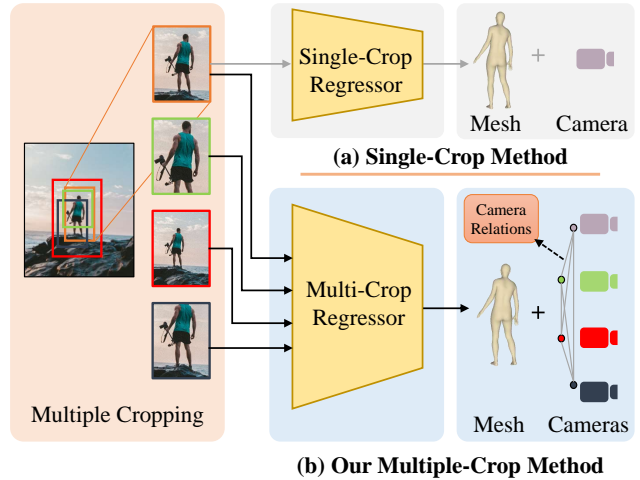


Figure 1. (a) **Previous single-crop HMR**: only one crop of the target human is used as the input to the regressor. (b) **Our multiple-crop HMR**: multiple crops are fed into the regressor to output the target mesh and multiple cameras with pairwise relations.

tract discriminative features from the input, and second it faces the ambiguity from 2D to 3D. Previous approaches either propose sophisticated networks for extracting better features (e.g., pixel-aligned [63, 64] and attention-based approaches [6, 8, 32, 33]), or alleviate ambiguity by imposing kinematic constraints [27, 28, 48] and building more accurate camera model [30, 54]. However, there is rare work tackling the two challenges simultaneously.

In this paper, we propose a novel and simple method to handle the above two challenges. Our key observation is that all previous approaches use a single cropped image as input (see Figure 1 (a)). Differently, we propose to crop multiple patches of the human and use them as input to regress the target mesh (see Figure 1 (b)).

It is worth emphasizing that the multiple cropping is feasible in practice due to the existence of the full-view image and the originally detected bounding box of the target

human, and is easy in implementation without much additional cost. Meanwhile, they provide more visual details to the network, and we can leverage the relation between the multiple crops to extract discriminative features and alleviate camera ambiguities.

The first relation we can leverage is that these multiple crops contain the same human with the same pose and shape. Therefore, we adopt contrastive learning to extract similar features from these crops. This idea is straightforward, as the content of these crops is dominated by the foreground human rather than the background. Constrained by the contrastive learning loss, the network is encouraged to focus on the foreground human and extract discriminative features for different human with different actions.

Second, different crops contain slightly different information about the target human. It is therefore beneficial to fuse the features of different crops for regressing the target mesh. Simple fusion strategies cannot align these features well and yield unsatisfactory results. We propose a crop-aware fusion method guided by the relative position of the bounding boxes of the crops, which performs the best among all the attempted fusion schemes.

Third and more importantly, the ambiguity of camera largely affects the accuracy of the estimated human meshes [30, 54]. With multiple crops, we can estimate multiple local cameras corresponding to the multiple cropped images (Figure 1 (b)). Since different crops share the same global camera of the full image, we analytically derive the pairwise relations between local cameras. This finally enables us to propose a camera-consistency loss to reduce the ambiguity of estimated cameras, which in turn improves the accuracy of the regression.

Overall, our method is simple and straightforward, yet very effective. Every component of our design plays a role in improving the regression results. In summary, our contributions include:

- We extend the traditional single-crop HMR paradigm to the proposed multiple-crop HMR.
- To fully leverage the information in multiple crops, we propose a regression network composing of a contrastive learning module, a crop-aware fusion module and a camera-consistency loss.
- Our method is simple and effective, surpassing the latest developments in this field on popular benchmarks.

2. Related Work

Single-Crop HMR. Most existing approaches recover human mesh from an image in a top-down manner, i.e., cropping persons from the image and estimating the human mesh in each cropped image separately. To solve this single-crop HMR problem, there are optimization-based approaches [3, 9, 44], regression-based approaches [19, 20, 26, 30, 43, 53, 65], and hybrid approaches [10, 16, 18, 26–

28, 48, 63]. Optimization approaches either directly fit parameters of a SMPL-based model [37, 42, 44, 46] to 2D joints in the input image [3, 44], or fine-tune a pre-trained regression network to match 2D evidences while utilizing priors learned by the network [18]. Different from optimization-based approaches, regression approaches directly train a model to extract features from an input image and map the features to a human mesh model, using CNN [20, 30, 43, 65], GCN [7, 22, 41], or Transformer [6, 8, 33, 34, 51, 56]. Many approaches combine regression and optimization methods. Just to name a few, work of [18, 26] get an initial prediction through regression-based methods and iteratively optimize the result making it in line with 2D-keypoints reprojection loss. Taking human-kinematics into consideration, work of [27, 28, 48] incorporate Inverse Kinematics Process with the neural network and iteratively update the rotation and location of each joint. All the mentioned approaches are single-crop based. In this paper, we extend regression-based approaches [19] and [30] to accept multiple crops as input.

HMR with More Than One Single Input. Considering that HMR is a task with much ambiguity, many methods tend to add more auxiliary information at the input end to better assist the network to reconstruct the accurate body mesh. Some methods manage to estimate the mesh with the aid of extra inputs such as 2D segmentation or silhouettes of the target human [12, 24, 57, 59, 62, 67] which help the network grasp and understand the human bodies in images with those guidance. Work of [36, 38, 61] try to utilize available sparse 3D markers on surface of the target human before full-body reconstruction and complete the dense human meshes through optimization or interpolation. There are also multi-view methods, by which the ambiguity of HMR is alleviated since multiple view angles and camera parameters are available [29, 45, 47, 49]. A large number of temporal (video-based) methods incorporate auxiliary inputs as well, such as trajectory [11, 60], optical flows [31] and 3D scene point cloud [66]. Different from the above multi-view or video-based approaches, the original input to our network is only one image. We just crop the input image multiple times, which is more convenient than extracting silhouettes or segmentations of human.

Camera Matters. From a different perspective, there exists work focusing on the camera projection model since it is the vital bridge between the image in the x-y plane and the mesh in the 3D space. Based on SPIN [26] and Simplify [3], the work of [23] optimizes the full perspective camera of the original full image. [25] tries to estimate the real camera pitch and yaw angles along with the mesh prediction and utilize them for the calculation of 2D-reprojection loss. [30] digs deeper into the full-image reprojection and uses bounding box information in order to guide the network towards the accurate full camera. [54] introduces a new dataset and

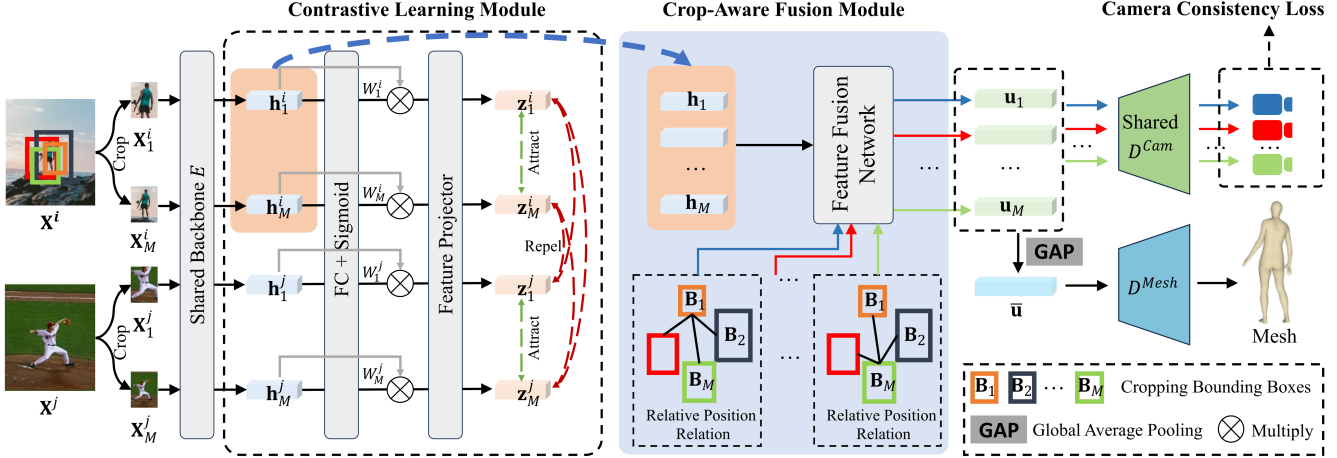


Figure 2. **Overview of our method.** Given a full image \mathbf{I}^i (or \mathbf{I}^j), we crop M patches $\{\mathbf{X}_m^i\}_{m=1}^M$ of a person in the image, and use a shared encoder E to extract features $\{\mathbf{h}_m^i\}_{m=1}^M$. We further project the features to $\{\mathbf{z}_m^i\}_{m=1}^M$, and apply a contrastive loss on \mathbf{z} in the same training batch. After that, we propose a crop-aware fusion module to fuse $\{\mathbf{h}_m\}_{m=1}^M$ (the superscript i is dropped) to obtain the fused features $\{\mathbf{u}_m\}_{m=1}^M$, under the guidance of relative position relation between bounding boxes $\{\mathbf{B}_m\}_{m=1}^M$. We finally use a shared decoder D^{cam} to decode each of the fused feature to a camera, and use a decoder D^{mesh} to decode the average fused feature $\bar{\mathbf{u}}$ to a human mesh.

copies with the scenario where people are shown up close in the image, taking the distortion of perspective projection into consideration. We, in this paper, model the pairwise relations between cameras estimated from different cropped images of the same person. This encourages the estimation of more accurate cameras.

3. Method

Since they are related to our method, we first review the seminar end-to-end HMR method [19] and the recently proposed state-of-the-art (SOTA) method CLIFF [30]. Both of them are single-crop HMR methods, based on which we introduce our multiple-crop HMR method.

3.1. Single-Crop HMR

Let \mathbf{I} be a full-view image, and \mathbf{X} (the resolution of which is 224×224 after resizing) be a detected and cropped human from \mathbf{I} . The seminar HMR method [19] learns a regression function f that maps \mathbf{X} to the parameters of a SMPL human mesh and a camera:

$$\theta, \beta, \mathbf{C} = f(\mathbf{X}), \quad (1)$$

where $\theta \in \mathbb{R}^{24 \times 3}$ determines the pose of the human mesh, $\beta \in \mathbb{R}^{10}$ determines the shape of the human mesh, and $\mathbf{C} = (s, t_x, t_y)$ contains scale and translation variables determining a weak-perspective camera that projects a 3D mesh onto the 2D image plane.

CLIFF [30] improves HMR [19] by additionally feeding the bounding box information $\mathbf{B} = (c_x, c_y, b)$ to the regression function:

$$\theta, \beta, \mathbf{C} = f(\mathbf{X}, \mathbf{B}), \quad (2)$$

where (c_x, c_y) is the location of the bounding box in the full-view image, and b is the width of the bounding box.

The estimated camera \mathbf{C} is the local camera specific to the cropped image. Another contribution of CLIFF is that they transform the local camera to the full-view camera of \mathbf{I} , and design training losses with respect to the global camera. We follow this to define training losses in the full image, and take a step further by using the global camera as a bridge to build pairwise relations between multiple local cameras.

3.2. Our Multiple-Crop HMR

Our main contribution is the following multiple-crop HMR paradigm. Let $\{\mathbf{X}_m\}_{m=1}^M$ be the M different crops of the same detected human, and $\{\mathbf{B}_m\}_{m=1}^M$ the corresponding bounding boxes of the crops, we formulate the following regression problem:

$$\theta, \beta, \{\mathbf{C}_m\}_{m=1}^M = f(\{\mathbf{X}_m\}_{m=1}^M, \{\mathbf{B}_m\}_{m=1}^M), \quad (3)$$

i.e. we input M crops and the corresponding M bounding boxes for the regression. We stress that we only regress one 3D mesh (θ, β) shared by all the cropped images as they capture the same human, while we regress different cameras $\{\mathbf{C}_m\}_{m=1}^M$ for different crops.

3.2.1 Cropping Method

Given one source image \mathbf{I} that contains at least one human body, most literature typically use bounding box $\mathbf{B} = (c_x, c_y, b)$ to indicate the location of the target human, which can be obtained either from annotation or from off-the-shelf detectors [14, 17]. Conventionally, only one

patch is cropped out according to \mathbf{B} . However, We exert cropping operation M times by different $\{\mathbf{B}_m\}_{m=1}^M$ based on the original \mathbf{B} , obtaining M cropped images $\{\mathbf{X}_m\}_{m=1}^M$. Specifically, each bounding box \mathbf{B}_m is obtained by slightly moving and scaling \mathbf{B} . In this paper, the offset that moves \mathbf{B} along the x and y axes includes $\{(0.1b, 0), (-0.1b, 0), (0, 0.1b), (0, -0.1b)\}$, and the corresponding scaling factors are $\{1.5, 1.25, 0.8, 0.65\}$ (see more details in the supplemental material). Together with the original bounding box, we totally crop $M = 5$ images of the human out of the full image. We have also tried randomly sampled bounding boxes, but obtained worse results. Please refer to the ablation studies for comparisons.

3.2.2 Our Network

Figure 2 shows the overall pipeline of the proposed method. Given $\{\mathbf{X}_m\}_{m=1}^M$ (the superscript i or j used in Figure 2 is dropped for simplicity), we use a shared encoder E to extract features from each cropped image, *i.e.* $\mathbf{h}_m = E(\mathbf{X}_m)$ for each m . Then, the features $\{\mathbf{h}_m\}_{m=1}^M$ undergo a contrastive learning module, where we first project $\{\mathbf{h}_m\}_{m=1}^M$ to $\{\mathbf{z}_m\}_{m=1}^M$, and then apply a contrastive loss on \mathbf{z} in the same training batch. After that, we use a crop-aware fusion module to fuse $\{\mathbf{h}_m\}_{m=1}^M$ together, obtaining fused features $\{\mathbf{u}_m\}_{m=1}^M$. The fusion is performed for each crop image separately, guided by the relative position relation between the bounding boxes $\{\mathbf{B}_m\}_{m=1}^M$. Finally, on one hand, we use a shared regression head D^{cam} to decode the fused features to their corresponding cameras:

$$\mathbf{C}_m = D^{cam}(\mathbf{u}_m), \forall m \in [1, M], \quad (4)$$

and impose a camera-consistency loss on all the estimated cameras $\{\mathbf{C}_m\}_{m=1}^M$. On the other hand, we employ another head D^{mesh} that takes the average of the fused features $\bar{\mathbf{u}}$ as input to output a 3D mesh shared by all the cropped images:

$$\theta, \beta = D^{mesh}(\bar{\mathbf{u}}). \quad (5)$$

3.2.3 Contrastive Learning Module

The first benefit of using multiple crops as input is that we can apply contrastive learning to encourage learning discriminative features. During training, we input a batch of N samples into the encoder, and there are actually $M \times N$ images fed into the network, as for each sample there are M crops depicting the same human body. It is natural to require the network to extract similar features from the crops of the same person but dissimilar features from different samples. Enforcing this constraint on the learning process can make the network pay attention to the human itself.

We basically implement the contrastive learning module following SimCLR [4]. As shown in Figure 2, let \mathbf{X}^i (or \mathbf{X}^j) be the i^{th} sample in a training batch, and \mathbf{X}_m^i , where

$m \in [1, M]$, is a crop of sample i , and \mathbf{h}_m^i is the feature extracted by the encoder E from \mathbf{X}_m^i . We first use a linear layer together with a Sigmoid function to transform \mathbf{h}_m^i to a weighting vector $\mathbf{W}_m^i \in [0, 1]^d$, where d is the dimension of \mathbf{W} (and also \mathbf{h}). We then multiply the weight \mathbf{W}_m^i and the feature \mathbf{h}_m^i . Finally, we use the feature projector $g(\cdot)$ defined in SimCLR to get representation $\mathbf{z}_m^i \in \mathbb{R}^d$:

$$\mathbf{z}_m^i = g(\mathbf{W}_m^i \cdot \mathbf{h}_m^i). \quad (6)$$

We then impose the following contrastive loss on all the projected features in the same training batch:

$$\mathcal{L}_{contrast} = \sum_{i=1}^N \sum_{m=1}^M \frac{-1}{M-1} \sum_{j=1, j \neq m}^M \log \frac{\exp(\mathbf{z}_m^i \cdot \mathbf{z}_j^i / \tau)}{\sum_{l=1, l \neq i(m)}^M \exp(\mathbf{z}_m^i \cdot \mathbf{z}_l / \tau)} \quad (7)$$

where $\tau = 0.5$ is the temperature parameter, $l \neq i(m)$ indicates \mathbf{z}_l cannot be \mathbf{z}_m^i . By the contrastive loss, we increase similarity between \mathbf{z}_m^i and \mathbf{z}_j^i of sample i , while reducing the similarity between features from different samples.

Remark. We obtain \mathbf{h} and \mathbf{z} after contrastive learning. We have compared between them about which one is more suitable as input to the following modules, and found \mathbf{h} is better. We conjecture this is because \mathbf{h} are directly extracted from input images while \mathbf{z} may lose too much information.

3.2.4 Crop-Aware Fusion Module

Please be aware that \mathbf{h}_m , although refined by the contrastive learning module, just contains the information about the m^{th} crop. It is beneficial to fuse all features $\{\mathbf{h}_m\}_{m=1}^M$ for reasoning the 3D mesh shared by all crops.

It is better for the fusion to meet the two requirements: (1) The features shall be aligned before performing the fusion. (2) We want to compute different fused features for different crops, based on which we can estimate a local camera for each crop individually. In light of this, we propose our crop-aware fusion method.

We solve the above two problems by leveraging the bounding box information $\{\mathbf{B}_m\}_{m=1}^M$ to assist the fusion. First, we use the *relative* position relation between the bounding boxes to align the features of different crops. Second, to compute the fused feature specific to a crop, we only use the position relations relative to the target crop. For example, in the crop-aware fusion part of Figure 2, to compute the fused feature \mathbf{u}_1 (see blue arrows), we compute the relative relation between \mathbf{B}_1 and all other bounding boxes.

Specifically, the relative position relation is simply computed as the difference between pairwise bounding boxes after positional encoding:

$$\gamma_{mn} = \gamma(\mathbf{B}_m) - \gamma(\mathbf{B}_n), \quad (8)$$

where $\gamma(\cdot)$ is the position encoding function [40, 51]:

$$\gamma(p) = (p, \sin(\pi p), \cos(\pi p), \dots, \sin(2^L \pi p), \cos(2^L \pi p)), \quad (9)$$

which is applied to each of the three variables of \mathbf{B}_m (or \mathbf{B}_n). We set $L = 32$ in this paper.

Then, taking the m^{th} crop as example, the way to compute the fused feature \mathbf{u}_m is (see Figure 3):

$$\begin{aligned} \mathbf{u}_m &= \sum_{n=1}^M w_{mn} \mathbf{h}_n, \\ \{w_{mn}\}_{n=1}^M &= \text{Softmax}(\text{Linear}(\{\mathbf{F}_{mn}\}_{n=1}^M)) \\ \mathbf{F}_{mn} &= \text{Concat}(\mathbf{h}_n, \gamma_{mn}), \end{aligned} \quad (10)$$

where $w_{mn} \in [0, 1]$ is a scalar used to fuse features of multiple crops. To compute w_{mn} , we first concatenate the feature \mathbf{h}_n and the relative position relation γ_{mn} , and then send the concatenated feature to a linear layer to obtain a scalar, which is finally converted to w_{mn} by a Softmax function.

With \mathbf{u}_m , we use the camera decoder D^{cam} defined in Eq. 4 to output the camera \mathbf{C}_m specific to the m^{th} cropped image. We send $\bar{\mathbf{u}} = \text{AvgPool}(\{\mathbf{u}_m\}_{m=1}^M)$ to the mesh decoder D^{mesh} to output the shared 3D human mesh.

Remark. The utilization of the relative position relation is very important to the effectiveness of our method. With relative position relation, simple fully-connected (FC) layers suffice to compute the weights for the fusion. An alternative way for the fusion is to employ the self-attention mechanism [51]. However, the self-attention can only leverage the position information of the bounding boxes but not the relative position relation, which produces worse results (see more details in ablation Section 4.4). Another point worth noting is that the positional encoding is also useful in our method, and we validate this by ablation studies.

3.2.5 Crop Camera Consistency Loss

Now we have estimated M cameras which we refer to as *local cameras*. The third benefit multiple crops can provide is that we can establish pairwise relations among the M local cameras. Enforcing these relations during training can enhance the accuracy of the estimated human mesh.

To obtain the relations, we observe that there is a *full camera* with respect to the full-view image, and we can convert between local and full cameras. We establish the relations between local cameras using the full camera as the bridge. In the following, we directly present the relations between local cameras. The detailed derivations can be found in the supplementary material.

Specifically, let $\mathbf{C}_i = (s_i, t_{x_i}, t_{y_i})$ be the parameters of the i^{th} crop camera, and $\mathbf{B}_i = (c_{x_i}, c_{y_i}, b_i)$ be the bounding box of the i^{th} cropped image. The relation between camera

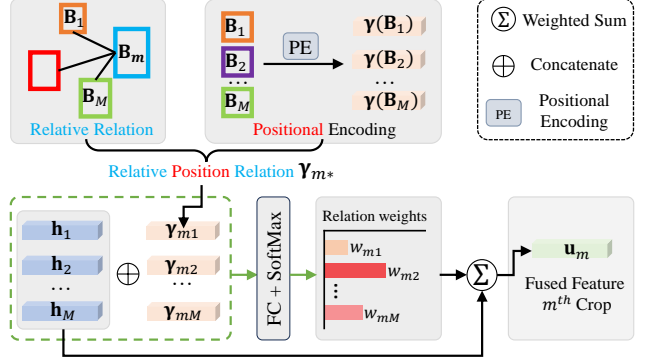


Figure 3. **Crop-aware fusion.** To obtain \mathbf{u}_m , we only consider the relative relation of other bounding boxes to the m^{th} bounding box. We perform positional encoding to all the bounding boxes and then compute relative position relation γ_{m*} (where $*$ is a number in $[1, M]$). We then concatenate γ_{m*} and the corresponding feature \mathbf{h}_* to compute weight w_{m*} . Finally, \mathbf{u}_m is the weighted sum of $\{\mathbf{h}_m\}_{m=1}^M$ with w_{m*} as the weights.

\mathbf{C}_i and \mathbf{C}_j is:

$$\begin{cases} t_{x_i} + \frac{2 \cdot c_{x_i}}{b_i \cdot s_i} = t_{x_j} + \frac{2 \cdot c_{x_j}}{b_j \cdot s_j} \\ t_{y_i} + \frac{2 \cdot c_{y_i}}{b_i \cdot s_i} = t_{y_j} + \frac{2 \cdot c_{y_j}}{b_j \cdot s_j} \\ b_i \cdot s_i = b_j \cdot s_j \end{cases} \quad (11)$$

Let

$$\begin{cases} \mathcal{L}_x(i, j) = \left\| \left(t_{x_i} + \frac{2 \cdot c_{x_i}}{b_i \cdot s_i} \right) - \left(t_{x_j} + \frac{2 \cdot c_{x_j}}{b_j \cdot s_j} \right) \right\|_2^2 \\ \mathcal{L}_y(i, j) = \left\| \left(t_{y_i} + \frac{2 \cdot c_{y_i}}{b_i \cdot s_i} \right) - \left(t_{y_j} + \frac{2 \cdot c_{y_j}}{b_j \cdot s_j} \right) \right\|_2^2 \\ \mathcal{L}_s(i, j) = \|b_i \cdot s_i - b_j \cdot s_j\|_2^2 \end{cases} \quad (12)$$

We establish the following camera consistency loss:

$$\mathcal{L}_{\text{cam}} = \sum_{i,j}^M \lambda_x \mathcal{L}_x(i, j) + \lambda_y \mathcal{L}_y(i, j) + \lambda_s \mathcal{L}_s(i, j). \quad (13)$$

3.3. Total Training Loss

Besides the contrastive loss in Eq. 7 and the camera consistency loss in Eq. 13, we also adopt the typical losses using GT mesh and 2D joints as supervision, including:

$$\begin{aligned} \mathcal{L}_{\text{smpl}} &= \|\Theta - \hat{\Theta}\|, \quad \mathcal{L}_{\text{vert}} = \|V^{3D} - \hat{V}^{3D}\|, \\ \mathcal{L}_{3D} &= \|J^{3D} - \hat{J}^{3D}\|_2^2, \quad \mathcal{L}_{2D} = \sum_m^M \|J_m^{2D} - \hat{J}_m^{2D}\|_2^2, \end{aligned} \quad (14)$$

where $\Theta = (\theta, \beta)$ denotes estimated SMPL parameters and $\hat{\Theta}$ is the ground truth, V^{3D} indicates 3D vertices of human mesh with \hat{V}^{3D} as the GT, and J^{3D} denotes the 3D joints of the human with \hat{J}^{3D} as the GT. For the 2D reprojection loss, $J_m^{2D} = \mathbf{C}'_m(J^{3D})$, where \mathbf{C}'_m is the full camera deduced from the local camera \mathbf{C}_m . Following [30], the projected

joints are compared with the GT 2D joints \hat{j}^{2D} in the full image. The total loss function is:

$$\mathcal{L}_{total} = \lambda_{cam}\mathcal{L}_{cam} + \lambda_{contrast}\mathcal{L}_{contrast} + \lambda_{smpl}\mathcal{L}_{smpl} + \lambda_{vert}\mathcal{L}_{vert} + \lambda_{3D}\mathcal{L}_{3D} + \lambda_{2D}\mathcal{L}_{2D}, \quad (15)$$

where λ_* are weights for each loss component and we basically set them following SPIN [26] except $\lambda_{contrast}$ and λ_{cam} , which are provided in supplemental material.

4. Experiments

4.1. Datasets and Metrics

To conduct fair comparison between our method and SOTA methods, we follow the dataset setting used in SOTA works [2, 5, 6, 24, 27, 63]. Specifically, we train our method on a mixture of four datasets including Human3.6M [15], MPI-INF-3DHP [39], COCO [35], and MPII [1].

As for evaluation, we use the test sets of 3DPW [52] and Human3.6M [15]. Following prior works, we finetune our model on 3DPW train set when evaluating on its test set.

We use MPJPE (Mean Per Joint Position Error [15]), PA-MPJPE (Procrustes-Aligned MPJPE [68]) and PVE (the mean Euclidean distance between mesh vertices) as the evaluation metrics.

4.2. Implementation Details

We implement our method using PyTorch. For the shared backbone, we use ResNet-50 [13] extracting features of $d = 2048$ dimensions and HRNet-W48 [50] extracting features of $d = 720$ dimensions, and refer to our methods with these backbones as Ours^{R50} and Ours^{H48}, respectively. Following [2, 54], we use the backbones that are pre-trained on COCO [35] for 2D pose estimation. We train our models with a learning rate of 1e-4 and 5e-5 for ResNet and HRNet backbones respectively, both scheduled by an Adam optimizer with $\beta_1 = 0.9$ and $\beta_2 = 0.999$. The batch-size for Ours^{R50} is 48 and that for Ours^{H48} is 20. Training with ResNet-50 takes around 25 epochs for 1 day and training with HRNet-W48 takes around 15 epochs for 2 days on NVIDIA RTX 3090. When finetuning on 3DPW, we fix the learning rate at 1e-5 (for both backbones) to train our models for another 5 epochs. By default, we use $M = 5$ crops.

4.3. Comparison to Prior Arts

In Table 1, we provide quantitative comparisons with SOTA approaches. We compare with various kinds of approaches including IK-based approaches [27, 28], iterative fitting approaches [55, 63, 64], Transformer-based approaches [6, 58], and approaches caring about camera [30, 54]. As seen, our method, either with a HRNet backbone or with a ResNet backbone, has better performance on the two evaluation datasets than the corresponding compared approaches.

| Method | 3DPW | | | Human3.6M | |
|---------------------------------|-------------|-------------|-------------|-------------|-------------|
| | MPJPE | PA-MPJPE | PVE | MPJPE | PA-MPJPE |
| HMR ^{R50} [19]’18 | 116.5 | 72.6 | — | — | 56.8 |
| SPIN ^{R50} [26]’19 | 96.9 | 59.2 | 116.4 | — | 41.1 |
| SPEC ^{R50} [25]’21 | 96.4 | 52.7 | — | — | — |
| PyMAF ^{R50} [63]’21 | 92.8 | 58.9 | 110.1 | 57.7 | 40.5 |
| PARE ^{R50} [24]’21 | 82.9 | 52.3 | 99.7 | — | — |
| PARE ^{H32} [24]’21 | 74.5 | 46.5 | 88.6 | — | — |
| Hybrik ^{R34} [27]’21 | 74.1 | 45.0 | 86.5 | 55.4 | 33.6 |
| FastMETRO ^{R50} [6]’22 | 77.9 | 48.3 | 90.6 | 53.9 | 37.3 |
| FastMETRO ^{H64} [6]’22 | 73.5 | 44.6 | 84.1 | 52.2 | 33.7 |
| CLIFF ^{R50} [30]’22 | 71.4 | 45.4 | 84.2 | 50.2 | 35.9 |
| CLIFF ^{H48} [30]’22 | 69.0 | 43.0 | 81.2 | 47.1 | 32.7 |
| MPT ^{H48} [34]’22 | 65.9 | 42.8 | 79.4 | 45.3 | 31.7 |
| PLIKS ^{H32} [48]’23 | 66.9 | 42.8 | 82.6 | 49.3 | 34.7 |
| BoPR ^{H48} [5]’23 | 65.4 | 42.5 | 80.8 | — | — |
| ReFit ^{H48} [55]’23 | 65.8 | 41.0 | — | 48.4 | 32.2 |
| Deformer ^{R50} [58]’23 | — | — | — | 50.7 | 36.3 |
| Deformer ^{H48} [58]’23 | 72.9 | 44.3 | 82.6 | 44.8 | 31.6 |
| PyMAF-X ^{R50} [64]’23 | 76.8 | 46.8 | 88.7 | 58.1 | 40.2 |
| PyMAF-X ^{H48} [64]’23 | 74.2 | 45.3 | 87.0 | 54.2 | 37.2 |
| NIKI ^{H48} [28]’23 | 71.3 | 40.6 | 86.6 | — | — |
| Zolly ^{R50} [54]’23 | 72.5 | 44.1 | 84.3 | 52.7 | 34.2 |
| Zolly ^{H48} [54]’23 | 67.2 | 40.9 | 78.4 | 49.4 | 32.3 |
| Ours ^{R50} | 68.2 | 43.2 | 81.9 | 45.4 | 33.0 |
| Ours ^{H48} | 64.1 | 40.4 | 78.6 | 42.2 | 30.7 |

Table 1. **Quantitative comparison with SOTA methods.** R50 (or R34) means using the backbone of ResNet [13]. H48 (or H32, H64) represents backbone of HRNet [50].

Please pay attention to the comparison between our method and CLIFF [30], as CLIFF can be viewed as the single-crop version of our method. Taking the backbone of HRNet-W48 as an example, the margin on MPJPE between CLIFF and ours is nearly 5mm, which is a significant improvement considering CLIFF is a very strong baseline. It is worth noting that our method works well in terms of all the three evaluation metrics, while Zolly [54] and NIKI [28] are competitive in terms of PA-MPJPE but not MPJPE or PVE. Our method performs well on both testing datasets, while other approaches such as PLIKS [48] and ReFit [55] show advantages on 3DPW but not Human3.6M. These experiments demonstrate the robustness of our method.

In Figure 4, we show qualitative comparisons between our method and SOTA approaches. The shown cases are challenging, which either contain complex poses or some part of the body is occluded by other body parts. For these cases, our estimated meshes resemble the GT (green color) better than results of the compared approaches. Figure 5 shows the action and per joint comparisons on Human3.6M. Our method outperforms FastMETRO and CLIFF on almost all kinds of actions and joints.

4.4. Ablation Study

In this section, we conduct ablation studies on the core design ideas of our method. All the following ablation studies



Figure 4. **Qualitative comparison with SOTA approaches.** The shown cases are challenging as they either own complex poses or some body parts are occluded and cannot be seen. Our results match better with the GT mesh (green) than other results.

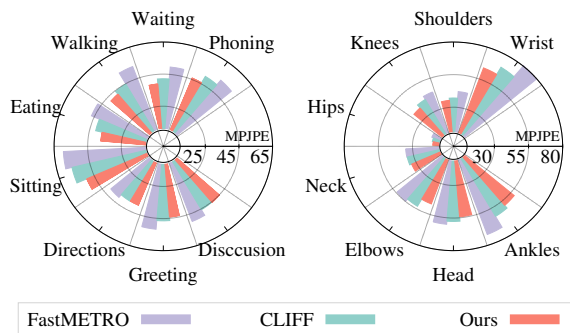


Figure 5. **Per action (left) or joint (right) MPJPE comparison** with FastMETRO [6] and CLIFF [30] on Human3.6M.

are performed on the COCO training dataset and tested on 3DPW, if not otherwise specified.

Core Components. Our method is composed of three major components: contrastive learning module (CLM), crop-aware fusion module (CAF), and camera consistency loss (CamLoss). To show the effect of each component, we remove each of them at a time while maintaining the other two components. See in Table 2 that removing any component incurs a large performance drop. Furthermore, we remove all the three components, making our method degenerate to CLIFF. Our method with two of the three components can outperform CLIFF.

Number of Crops. An interesting point is how the number of crops influences the regression accuracy. We conduct an ablation study that gradually increases the number of in-

| CLM | CAF | CamLoss | MPJPE | PA-MPJPE |
|-----|-----|---------|-------------|-------------|
| ✗ | ✗ | ✗ | 84.6 | 54.2 |
| ✗ | ✓ | ✓ | 83.4 | 53.3 |
| ✓ | ✗ | ✓ | 83.8 | 54.8 |
| ✓ | ✓ | ✗ | 83.1 | 52.0 |
| ✓ | ✓ | ✓ | 80.8 | 51.9 |

Table 2. **Ablation on core components of our method.**

| Crop Num | 1 | 2 | 3 | 4 | 5 |
|--|-------------|-------|-------|-------|-------------|
| | crop | crops | crops | crops | crops |
| MPJPE (mm) | 84.6 | 82.9 | 81.2 | 82.2 | 80.8 |
| PA-MPJPE (mm) | 54.2 | 54.4 | 52.3 | 53.1 | 51.9 |
| Final \mathcal{L}_{2D} ($\times 1e-3$) | 1.6 | 1.8 | 1.9 | 2.3 | 2.4 |
| Inferring speed (<i>fps</i>) | 76.3 | 63.5 | 61.7 | 57.3 | 55.6 |

Table 3. **Ablation on number of input crops.** Five is the default.

put crops in Table 3. As seen, the accuracy is consistently increased as the number of input crops increases. Experiments of inputting 6 or more crops are not conducted due to memory limit. We find that as the crop number increases, the \mathcal{L}_{2D} loss per crop increases too, but we obtain higher regression accuracy. This may indicate that inputting more crops prevents the network from over-fitting problem.

Inferring Speed. We also report the inferring speed in Table 3. As the number of crops increases, the inferring speed is just slightly decreased. With 5 crops, our method processes 55.6 frames per second, which is still fast.

| Bounding box | Scaling | Shifting | MPJPE | PA-MPJPE |
|--------------|--------------|--------------|-------------|-------------|
| Fixed | \times | \times | 83.6 | 54.4 |
| | \checkmark | \times | 83.4 | 53.3 |
| | \times | \checkmark | 83.1 | 52.0 |
| | \checkmark | \checkmark | 80.8 | 51.9 |
| Random | \checkmark | \checkmark | 84.4 | 54.1 |

Table 4. **Ablation on cropping method.** “Fixed”: the relative positions of cropped bounding boxes with respect to the originally detected one are the same across different training/testing samples. “Random”: the relative positions are different per sample.

Cropping Method. We slightly shift and scale the originally detected bounding box of a human to obtain new bounding boxes for cropping the human. By default, the relative shifting offsets and scaling factors are the same across different samples. We call this “Fixed” cropping with scaling and shifting. Table 4 shows many other cropping schemes. For example, “Fixed” w/o scaling and w/o shifting simply repeats the original bounding box multiple times. By “Random cropping”, we randomly generate bounding boxes around the original one. As seen, the default manner gives the best result. Repeated cropping degrades to only one input. Random cropping may increase the difficulty of network learning. Since shifting and scaling increase the diversity of camera relations, they are both benefit for the final estimation accuracy.

Importance of Relative Relation and Positional Encoding. We rely on relative relation for the crop-aware feature fusion, and the relation is computed based on the positional encoding (PE) of the bounding boxes. Both of them are critical to our method, as shown in Table 5. We test concatenating (see the “concatenate” operator in Figure 3) no information (*i.e.*, $\mathbf{h}_* \oplus \text{NULL}$ which uses \mathbf{h}_* only for computing the corresponding weight), concatenating PE of the crop itself (*i.e.* not using relative relation), and concatenating the relative PE information (*i.e.*, $\mathbf{h}_* \oplus \gamma_{m*}$) with different length L of PE. As seen, the relative PE with $L = 32$ yields the best results.

We have also implemented the crop-aware fusion by performing self attention [51] on M tokens of $\{\mathbf{h}_m \oplus \gamma(\mathbf{B}_m)\}_{m=1}^M$. Here we can only concatenate PE but not relative PE, since there is only M tokens but we have M^2 relative relations (see supplemental material for details). Results are shown in Figure 6, where our relative-PE based scheme (CAF) outperforms the self-attention approach.

4.5. Limitations

Figure 7 shows failure cases, where both our method and CLIFF produce nearly perfect reprojection results without noticeable misalignment in the 2D image. But in the 3D space, though our method is better than CLIFF, some body

| Concatenation | L of PE | MPJPE | PA-MPJPE |
|--|-----------|-------------|-------------|
| $\mathbf{h}_* \oplus \text{NULL}$ | — | 98.7 | 56.9 |
| $\mathbf{h}_* \oplus \gamma(\mathbf{B}_*)$ | $L = 32$ | 87.6 | 55.0 |
| $\mathbf{h}_* \oplus \gamma_{m*}$ | $L = 0$ | 81.6 | 52.9 |
| $\mathbf{h}_* \oplus \gamma_{m*}$ | $L = 32$ | 80.8 | 51.9 |
| $\mathbf{h}_* \oplus \gamma_{m*}$ | $L = 64$ | 81.1 | 52.3 |

Table 5. **Importance of Relative Relation and Positional Encoding (PE).** (1) $\mathbf{h}_* \oplus \text{NULL}$: concatenating nothing, *i.e.*, using feature \mathbf{h}_* only for computing relation weights, where $*$ is a number in $[1, M]$. (2) $\mathbf{h}_* \oplus \gamma(\mathbf{B}_*)$: concatenating PE of the corresponding bounding box. (3) $\mathbf{h}_* \oplus \gamma_{m*}$: concatenating relative PE γ_{m*} for computing m^{th} fused feature. (4) L is the length of PE.

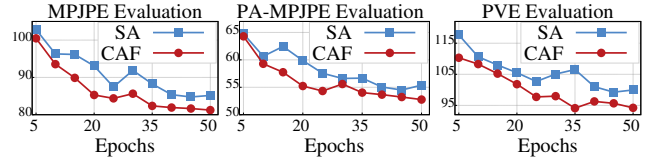


Figure 6. **Comparison between self-attention-based fusion and our proposed relative-relation-based fusion (CAF).** Regression accuracy at different training epochs are shown.

parts of both methods deviate from the ground truth. These examples further show that our method outperforms CLIFF. But as a single-image method, introducing multiple crops still cannot solve the ill-posed problem that there are multiple 3D meshes matching with the same 2D person.

5. Conclusion and Future Work

This paper digs into the relation among different crops of the same person in an image for human mesh recovery. With the multiple cropped images via different cropping centers and scales, we are able to provide three strategies to extract discriminative features and estimate reliable camera parameters, thanks to the additional visual information provided by the multiple inputs. Specifically, we have exploited the using of contrastive learning, relative-position-relation guided feature fusion, and camera-consistency loss to take advantage of the information in multiple inputs as much as possible. We validate the effectiveness of each proposed component using abundant experiments and prove our method has better regression accuracy than current SOTA approaches on popular benchmarks and datasets. In the future, it is valuable to investigate whether the proposed strategies are effective in multi-view or video-based HMR.

References

- [1] Mykhaylo Andriluka, Leonid Pishchulin, Peter Gehler, and Bernt Schiele. 2d human pose estimation: New benchmark and state of the art analysis. In *Proceedings of the IEEE Con-*

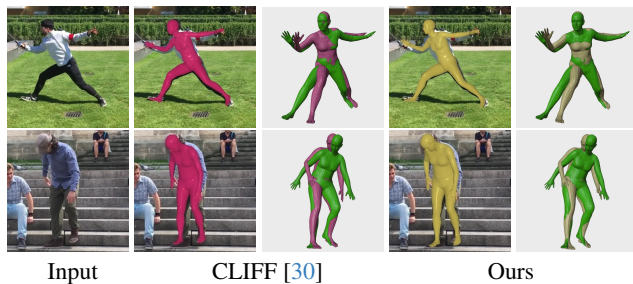


Figure 7. **Failure examples.** Both our method and CLIFF produce nearly perfect results in the 2D image, but not in the 3D space.

- ference on computer Vision and Pattern Recognition*, pages 3686–3693, 2014. 6
- [2] Michael J Black, Priyanka Patel, Joachim Tesch, and Jinlong Yang. Bedlam: A synthetic dataset of bodies exhibiting detailed lifelike animated motion. In *Proceedings of the IEEE/CVF Conference on Computer Vision and Pattern Recognition*, pages 8726–8737, 2023. 6
- [3] Federica Bogo, Angjoo Kanazawa, Christoph Lassner, Peter Gehler, Javier Romero, and Michael J Black. Keep it smpl: Automatic estimation of 3d human pose and shape from a single image. In *Computer Vision–ECCV 2016: 14th European Conference, Amsterdam, The Netherlands, October 11–14, 2016, Proceedings, Part V 14*, pages 561–578. Springer, 2016. 2
- [4] Ting Chen, Simon Kornblith, Mohammad Norouzi, and Geoffrey Hinton. Simclr: A simple framework for contrastive learning of visual representations. In *International Conference on Learning Representations*, 2020. 4
- [5] Yongkang Cheng, Shaoli Huang, Jifeng Ning, and Ying Shan. Bopr: Body-aware part regressor for human shape and pose estimation. *arXiv preprint arXiv:2303.11675*, 2023. 6
- [6] Junhyeong Cho, Kim Youwang, and Tae-Hyun Oh. Cross-attention of disentangled modalities for 3d human mesh recovery with transformers. In *European Conference on Computer Vision*, pages 342–359. Springer, 2022. 1, 2, 6, 7
- [7] Hongsuk Choi, Gyeongsik Moon, and Kyoung Mu Lee. Pose2mesh: Graph convolutional network for 3d human pose and mesh recovery from a 2d human pose. In *Computer Vision–ECCV 2020: 16th European Conference, Glasgow, UK, August 23–28, 2020, Proceedings, Part VII 16*, pages 769–787. Springer, 2020. 2
- [8] Zhiyang Dou, Qingxuan Wu, Cheng Lin, Zeyu Cao, Qiangqiang Wu, Weilin Wan, Taku Komura, and Wenping Wang. Tore: Token reduction for efficient human mesh recovery with transformer. *arXiv preprint arXiv:2211.10705*, 2022. 1, 2
- [9] Taosha Fan, Kalyan Vasudev Alwala, Donglai Xiang, Weipeng Xu, Todd Murphey, and Mustafa Mukadam. Revitalizing optimization for 3d human pose and shape estimation: A sparse constrained formulation. In *Proceedings of the IEEE/CVF International Conference on Computer Vision*, pages 11457–11466, 2021. 2
- [10] Qi Fang, Kang Chen, Yinghui Fan, Qing Shuai, Jiefeng Li, and Weidong Zhang. Learning analytical posterior probability for human mesh recovery. In *Proceedings of the IEEE/CVF Conference on Computer Vision and Pattern Recognition*, pages 8781–8791, 2023. 2
- [11] Shubham Goel, Georgios Pavlakos, Jathushan Rajasegaran, Angjoo Kanazawa, and Jitendra Malik. Humans in 4d: Reconstructing and tracking humans with transformers. In *Proceedings of the IEEE international conference on computer vision*, 2023. 2
- [12] Peng Guan, Alexander Weiss, Alexandru O Balan, and Michael J Black. Estimating human shape and pose from a single image. In *2009 IEEE 12th International Conference on Computer Vision*, pages 1381–1388. IEEE, 2009. 2
- [13] Kaiming He, Xiangyu Zhang, Shaoqing Ren, and Jian Sun. Identity mappings in deep residual networks. In *Computer Vision–ECCV 2016: 14th European Conference, Amsterdam, The Netherlands, October 11–14, 2016, Proceedings, Part IV 14*, pages 630–645. Springer, 2016. 6
- [14] Kaiming He, Georgia Gkioxari, Piotr Dollár, and Ross Girshick. Mask r-cnn. In *Proceedings of the IEEE international conference on computer vision*, pages 2961–2969, 2017. 3
- [15] Catalin Ionescu, Dragos Papava, Vlad Olaru, and Cristian Sminchisescu. Human3.6m: Large scale datasets and predictive methods for 3d human sensing in natural environments. *IEEE transactions on pattern analysis and machine intelligence*, 36(7):1325–1339, 2013. 6
- [16] Umar Iqbal, Kevin Xie, Yunrong Guo, Jan Kautz, and Pavlo Molchanov. Kama: 3d keypoint aware body mesh articulation. In *2021 International Conference on 3D Vision (3DV)*, pages 689–699. IEEE, 2021. 2
- [17] Glenn Jocher, Ayush Chaurasia, Alex Stoken, Jirka Borovec, Yonghye Kwon, Kalen Michael, Jiacong Fang, Zeng Yifu, Colin Wong, Diego Montes, et al. ultralytics/yolov5: v7. 0-yolov5 sota realtime instance segmentation. *Zenodo*, 2022. 3
- [18] Hanbyul Joo, Natalia Neverova, and Andrea Vedaldi. Exemplar fine-tuning for 3d human model fitting towards in-the-wild 3d human pose estimation. In *2021 International Conference on 3D Vision (3DV)*, pages 42–52. IEEE, 2021. 2
- [19] Angjoo Kanazawa, Michael J Black, David W Jacobs, and Jitendra Malik. End-to-end recovery of human shape and pose. In *Proceedings of the IEEE conference on computer vision and pattern recognition*, pages 7122–7131, 2018. 1, 2, 3, 6
- [20] Rawal Khirodkar, Shashank Tripathi, and Kris Kitani. Occluded human mesh recovery. In *Proceedings of the IEEE/CVF conference on computer vision and pattern recognition*, pages 1715–1725, 2022. 2
- [21] Prannay Khosla, Piotr Teterwak, Chen Wang, Aaron Sarna, Yonglong Tian, Phillip Isola, Aaron Maschinot, Ce Liu, and Dilip Krishnan. Supervised contrastive learning. *Advances in neural information processing systems*, 33:18661–18673, 2020.
- [22] Thomas N Kipf and Max Welling. Semi-supervised classification with graph convolutional networks. *arXiv preprint arXiv:1609.02907*, 2016. 2
- [23] Imry Kissos, Lior Fritz, Matan Goldman, Omer Meir, Edward Oks, and Mark Kliger. Beyond weak perspective for

- monocular 3d human pose estimation. In *Computer Vision–ECCV 2020 Workshops: Glasgow, UK, August 23–28, 2020, Proceedings, Part II 16*, pages 541–554. Springer, 2020. 2
- [24] Muhammed Kocabas, Chun-Hao P Huang, Otmar Hilliges, and Michael J Black. Pare: Part attention regressor for 3d human body estimation. In *Proceedings of the IEEE/CVF International Conference on Computer Vision*, pages 11127–11137, 2021. 2, 6
- [25] Muhammed Kocabas, Chun-Hao P Huang, Joachim Tesch, Lea Müller, Otmar Hilliges, and Michael J Black. Spec: Seeing people in the wild with an estimated camera. In *Proceedings of the IEEE/CVF International Conference on Computer Vision*, pages 11035–11045, 2021. 2, 6
- [26] Nikos Kolotouros, Georgios Pavlakos, Michael J Black, and Kostas Daniilidis. Learning to reconstruct 3d human pose and shape via model-fitting in the loop. In *Proceedings of the IEEE/CVF international conference on computer vision*, pages 2252–2261, 2019. 2, 6
- [27] Jiefeng Li, Chao Xu, Zhicun Chen, Siyuan Bian, Lixin Yang, and Cewu Lu. Hybrik: A hybrid analytical-neural inverse kinematics solution for 3d human pose and shape estimation. In *Proceedings of the IEEE/CVF conference on computer vision and pattern recognition*, pages 3383–3393, 2021. 1, 2, 6
- [28] Jiefeng Li, Siyuan Bian, Qi Liu, Jiasheng Tang, Fan Wang, and Cewu Lu. Niki: Neural inverse kinematics with invertible neural networks for 3d human pose and shape estimation. In *Proceedings of the IEEE/CVF Conference on Computer Vision and Pattern Recognition*, pages 12933–12942, 2023. 1, 2, 6
- [29] Zhongguo Li, Magnus Oskarsson, and Anders Heyden. 3d human pose and shape estimation through collaborative learning and multi-view model-fitting. In *Proceedings of the IEEE/CVF winter conference on applications of computer vision*, pages 1888–1897, 2021. 2
- [30] Zhihao Li, Jianzhuang Liu, Zhensong Zhang, Songcen Xu, and Youliang Yan. Cliff: Carrying location information in full frames into human pose and shape estimation. In *European Conference on Computer Vision*, pages 590–606. Springer, 2022. 1, 2, 3, 5, 6, 7, 9
- [31] Ziwen Li, Bo Xu, Han Huang, Cheng Lu, and Yandong Guo. Deep two-stream video inference for human body pose and shape estimation. In *Proceedings of the IEEE/CVF Winter Conference on Applications of Computer Vision*, pages 430–439, 2022. 2
- [32] Kevin Lin, Lijuan Wang, and Zicheng Liu. End-to-end human pose and mesh reconstruction with transformers. In *Proceedings of the IEEE/CVF conference on computer vision and pattern recognition*, pages 1954–1963, 2021. 1
- [33] Kevin Lin, Lijuan Wang, and Zicheng Liu. Mesh graphormer. In *Proceedings of the IEEE/CVF international conference on computer vision*, pages 12939–12948, 2021. 1, 2
- [34] Kevin Lin, Chung-Ching Lin, Lin Liang, Zicheng Liu, and Lijuan Wang. Mpt: Mesh pre-training with transformers for human pose and mesh reconstruction. *arXiv preprint arXiv:2211.13357*, 2022. 1, 2, 6
- [35] Tsung-Yi Lin, Michael Maire, Serge Belongie, James Hays, Pietro Perona, Deva Ramanan, Piotr Dollár, and C Lawrence Zitnick. Microsoft coco: Common objects in context. In *Computer Vision–ECCV 2014: 13th European Conference, Zurich, Switzerland, September 6–12, 2014, Proceedings, Part V 13*, pages 740–755. Springer, 2014. 6
- [36] Matthew Loper, Naureen Mahmood, and Michael J Black. Mosh: motion and shape capture from sparse markers. *ACM Trans. Graph.*, 33(6):220–1, 2014. 2
- [37] Matthew Loper, Naureen Mahmood, Javier Romero, Gerard Pons-Moll, and Michael J Black. Smpl: A skinned multi-person linear model. *ACM Transactions on Graphics*, 34(6), 2015. 1, 2
- [38] Naureen Mahmood, Nima Ghorbani, Nikolaus F. Troje, Gerard Pons-Moll, and Michael J. Black. Amass: Archive of motion capture as surface shapes. In *The IEEE International Conference on Computer Vision (ICCV)*, 2019. 2
- [39] Dushyant Mehta, Helge Rhodin, Dan Casas, Pascal Fua, Oleksandr Sotnychenko, Weipeng Xu, and Christian Theobalt. Monocular 3d human pose estimation in the wild using improved cnn supervision. In *2017 international conference on 3D vision (3DV)*, pages 506–516. IEEE, 2017. 6
- [40] Ben Mildenhall, Pratul P Srinivasan, Matthew Tancik, Jonathan T Barron, Ravi Ramamoorthi, and Ren Ng. Nerf: Representing scenes as neural radiance fields for view synthesis. *Communications of the ACM*, 65(1):99–106, 2021. 5
- [41] Gyeongsik Moon and Kyoung Mu Lee. I2l-meshnet: Image-to-lixel prediction network for accurate 3d human pose and mesh estimation from a single rgb image. In *Computer Vision–ECCV 2020: 16th European Conference, Glasgow, UK, August 23–28, 2020, Proceedings, Part VII 16*, pages 752–768. Springer, 2020. 2
- [42] Ahmed AA Osman, Timo Bolkart, and Michael J Black. Star: Sparse trained articulated human body regressor. In *Computer Vision–ECCV 2020: 16th European Conference, Glasgow, UK, August 23–28, 2020, Proceedings, Part VI 16*, pages 598–613. Springer, 2020. 2
- [43] Georgios Pavlakos, Luyang Zhu, Xiaowei Zhou, and Kostas Daniilidis. Learning to estimate 3d human pose and shape from a single color image. In *Proceedings of the IEEE conference on computer vision and pattern recognition*, pages 459–468, 2018. 2
- [44] Georgios Pavlakos, Vasileios Choutas, Nima Ghorbani, Timo Bolkart, Ahmed AA Osman, Dimitrios Tzionas, and Michael J Black. Expressive body capture: 3d hands, face, and body from a single image. In *Proceedings of the IEEE/CVF conference on computer vision and pattern recognition*, pages 10975–10985, 2019. 2
- [45] Georgios Pavlakos, Jitendra Malik, and Angjoo Kanazawa. Human mesh recovery from multiple shots. In *Proceedings of the IEEE/CVF Conference on Computer Vision and Pattern Recognition*, pages 1485–1495, 2022. 2
- [46] Javier Romero, Dimitrios Tzionas, and Michael J Black. Embodied hands: Modeling and capturing hands and bodies together. *arXiv preprint arXiv:2201.02610*, 2022. 2
- [47] Akash Sengupta, Ignas Budvytis, and Roberto Cipolla. Probabilistic 3d human shape and pose estimation from multi-

- ple unconstrained images in the wild. In *Proceedings of the IEEE/CVF Conference on Computer Vision and Pattern Recognition*, pages 16094–16104, 2021. 2
- [48] Karthik Shetty, Annette Birkhold, Srikrishna Jaganathan, Norbert Strobel, Markus Kowarschik, Andreas Maier, and Bernhard Egger. Pliks: A pseudo-linear inverse kinematic solver for 3d human body estimation. In *Proceedings of the IEEE/CVF Conference on Computer Vision and Pattern Recognition*, pages 574–584, 2023. 1, 2, 6
- [49] S Shin and E Halilaj. Multi-view human pose and shape estimation using learnable volumetric aggregation. *arxiv.org*. *arXiv preprint arXiv:2011.13427*, 2020. 2
- [50] Ke Sun, Bin Xiao, Dong Liu, and Jingdong Wang. Deep high-resolution representation learning for human pose estimation. In *Proceedings of the IEEE/CVF conference on computer vision and pattern recognition*, pages 5693–5703, 2019. 6
- [51] Ashish Vaswani, Noam Shazeer, Niki Parmar, Jakob Uszkoreit, Llion Jones, Aidan N Gomez, Łukasz Kaiser, and Illia Polosukhin. Attention is all you need. *Advances in neural information processing systems*, 30, 2017. 2, 5, 8
- [52] Timo Von Marcard, Roberto Henschel, Michael J Black, Bodo Rosenhahn, and Gerard Pons-Moll. Recovering accurate 3d human pose in the wild using imus and a moving camera. In *Proceedings of the European conference on computer vision (ECCV)*, pages 601–617, 2018. 6
- [53] Nanyang Wang, Yinda Zhang, Zhuwen Li, Yanwei Fu, Wei Liu, and Yu-Gang Jiang. Pixel2mesh: Generating 3d mesh models from single rgb images. In *Proceedings of the European conference on computer vision (ECCV)*, pages 52–67, 2018. 2
- [54] Wenjia Wang, Yongtao Ge, Haiyi Mei, Zhongang Cai, Qingping Sun, Yanjun Wang, Chunhua Shen, Lei Yang, and Taku Komura. Zolly: Zoom focal length correctly for perspective-distorted human mesh reconstruction. *arXiv preprint arXiv:2303.13796*, 2023. 1, 2, 6
- [55] Yufu Wang and Kostas Daniilidis. Refit: Recurrent fitting network for 3d human recovery. In *Proceedings of the IEEE/CVF International Conference on Computer Vision*, pages 14644–14654, 2023. 6, 7
- [56] Youze Xue, Jiansheng Chen, Yudong Zhang, Cheng Yu, Huimin Ma, and Hongbing Ma. 3d human mesh reconstruction by learning to sample joint adaptive tokens for transformers. In *Proceedings of the 30th ACM International Conference on Multimedia*, pages 6765–6773, 2022. 2
- [57] Pengfei Yao, Zheng Fang, Fan Wu, Yao Feng, and Jiwei Li. Densebody: Directly regressing dense 3d human pose and shape from a single color image. *arXiv preprint arXiv:1903.10153*, 2019. 2
- [58] Yusuke Yoshiyasu. Deformable mesh transformer for 3d human mesh recovery. In *Proceedings of the IEEE/CVF Conference on Computer Vision and Pattern Recognition*, pages 17006–17015, 2023. 6
- [59] Zhenbo Yu, Junjie Wang, Jingwei Xu, Bingbing Ni, Chenglong Zhao, Minsi Wang, and Wenjun Zhang. Skeleton2mesh: Kinematics prior injected unsupervised human mesh recovery. In *Proceedings of the IEEE/CVF International Conference on Computer Vision*, pages 8619–8629, 2021. 2
- [60] Ye Yuan, Umar Iqbal, Pavlo Molchanov, Kris Kitani, and Jan Kautz. Glamr: Global occlusion-aware human mesh recovery with dynamic cameras. In *Proceedings of the IEEE/CVF conference on computer vision and pattern recognition*, pages 11038–11049, 2022. 2
- [61] Mihai Zanfir, Andrei Zanfir, Eduard Gabriel Bazavan, William T Freeman, Rahul Sukthankar, and Cristian Sminchisescu. Thundr: Transformer-based 3d human reconstruction with markers. In *Proceedings of the IEEE/CVF International Conference on Computer Vision*, pages 12971–12980, 2021. 2
- [62] Hongwen Zhang, Jie Cao, Guo Lu, Wanli Ouyang, and Zhenan Sun. Learning 3d human shape and pose from dense body parts. *IEEE Transactions on Pattern Analysis and Machine Intelligence*, 44(5):2610–2627, 2020. 2
- [63] Hongwen Zhang, Yating Tian, Xinchu Zhou, Wanli Ouyang, Yebin Liu, Limin Wang, and Zhenan Sun. Pymaf: 3d human pose and shape regression with pyramidal mesh alignment feedback loop. In *Proceedings of the IEEE/CVF International Conference on Computer Vision*, pages 11446–11456, 2021. 1, 2, 6
- [64] Hongwen Zhang, Yating Tian, Yuxiang Zhang, Mengcheng Li, Liang An, Zhenan Sun, and Yebin Liu. Pymaf-x: Towards well-aligned full-body model regression from monocular images. *IEEE Transactions on Pattern Analysis and Machine Intelligence*, 2023. 1, 6
- [65] Jianfeng Zhang, Dongdong Yu, Jun Hao Liew, Xuecheng Nie, and Jiashi Feng. Body meshes as points. In *Proceedings of the IEEE/CVF Conference on Computer Vision and Pattern Recognition*, pages 546–556, 2021. 2
- [66] Siwei Zhang, Qianli Ma, Yan Zhang, Sadegh Aliakbarian, Darren Cosker, and Siyu Tang. Probabilistic human mesh recovery in 3d scenes from egocentric views. *arXiv preprint arXiv:2304.06024*, 2023. 2
- [67] Tianshu Zhang, Buzhen Huang, and Yangang Wang. Object-occluded human shape and pose estimation from a single color image. In *Proceedings of the IEEE/CVF conference on computer vision and pattern recognition*, pages 7376–7385, 2020. 2
- [68] Xiaowei Zhou, Menglong Zhu, Georgios Pavlakos, Spyridon Leonardos, Konstantinos G Derpanis, and Kostas Daniilidis. Monocap: Monocular human motion capture using a cnn coupled with a geometric prior. *IEEE transactions on pattern analysis and machine intelligence*, 41(4):901–914, 2018. 6